nature communications

Article

https://doi.org/10.1038/s41467-024-51171-6

Time-reflection of microwaves by a fast optically-controlled time-boundary

Received: 18 February 2024

Accepted: 30 July 2024

Published online: 08 August 2024

Check for updates

Thomas R. Jones[1], Alexander V. Kildishev[1], Mordechai Segev[2] & Dimitrios Peroulis[1]

When an electromagnetic (EM) wave propagates in a medium whose properties are varied abruptly in time, the wave experiences refractions and reflections known as time-refractions and time-reflections, both manifesting spectral translation as a consequence of the abrupt change of the medium and the conservation of momentum. However, while the time-refracted wave continues to propagate with the same wave-vector, the time-reflected wave propagates backward with a conjugate phase despite the lack of any spatial interface. Importantly, while time-refraction is always significant, observing time-reflection poses a major challenge – because it requires a large change in the medium occurring within a single cycle of the EM wave. For that reason, time-reflection of EM waves was observed only recently. Here, we present the observation of microwave pulses at the highest frequency ever observed (0.59 GHz), and the experimental evidence of the phase-conjugation nature of time-reflected waves. Our experiments are carried out in a periodically-loaded microstrip line with optically-controlled picosecond-switchable photodiodes. Our system paves the way to the experimental realization of Photonic Time-Crystals at GHz frequencies.

When the refractive index of a medium changes abruptly in time, a wave propagating in the medium experiences time-refraction and time-reflection, similar to the refraction and reflection at dielectric interfaces[1–6]. However, despite the similarity, time-reflection and refraction are fundamentally different than their spatial counterparts. Namely, whereas energy (frequency) is conserved at spatial interfaces between dielectric media, a time-interface necessarily changes the frequency, because the temporal modulation breaks time-translation symmetry. On the other hand, when the abrupt temporal change occurs in a homogeneous medium, momentum (wave-vector k) is conserved, which implies that both the time-refraction and the time-reflection experience translation of their spectrum[4–6]. Also, causality implies that the time-reflection cannot go back in time (unfortunately) but instead is back-reflected in space. That is, while the time-refracted wave continues to propagate with the same wave-vector, the time-reflected wave starts propagating backward with a conjugate phase[1,6,7]. In this way, modulating the refractive index strongly and periodically in time gives rise to multiple time-reflections and time-refractions, which interfere and yield dispersion bands separated by bandgaps in the momentum k[8–12]. This temporal structure is known as Photonic Time-Crystals (PTCs). The most intriguing property of PTCs is that states residing in the momentum gap can have exponentially increasing amplitudes, which draw energy from the modulation[11,13–15]. PTCs offer a plethora of new possibilities for innovative physics and applications, ranging from the generation of pairs of entangled photons[14] and below-threshold Cherenkov radiation[16] to new widely-tunable laser sources at THz frequencies[17–24]. However, all of these rely on time-reflections: without significant time-reflections, there would be no PTCs. This understanding poses a major challenge: unlike time-refraction, which is (almost) always significant[3,25–28] for the time-reflection to be substantial, the refractive index change has to be large (order of unity) and abrupt (occurring within 1-2 cycles of the time-reflected waves)[27,28]. Otherwise, if the index change is insufficiently strong or too slow, then the time-reflection becomes extremely weak,

[1]Elmore Family School of Electrical and Computer Engineering, Purdue University, West Lafayette, IN, USA. [2]Department of Physics, Technion-Israel Institute of Technology, Haifa, Israel. e-mail: dperouli@purdue.edu

and realizing a PTC becomes completely impossible[28,29]. Such a tough requirement to have a strong and abrupt change in the refractive index simultaneously is the reason why the universal phenomenon of time-reflected waves was first studied with water waves[30] and only very recently with EM waves, demonstrating time-reflection at microwave frequencies[31]. In that particular study[31], time-reflection was demonstrated at ~50 MHz, and incident asymmetric pulses were observed to be time-reflected in reverse order. Additionally, the same work demonstrated two consecutive time-reflections, acting as the temporal analog of a Fabry–Perot filter.

Here, we study the propagation of microwaves in a periodically-loaded microstrip transmission line with optically-controlled picosecond-switchable photodiodes, and present time-reflection at the highest frequency ever observed (0.59 GHz) along with direct experimental evidence for its phase-conjugate nature. Our experiments display the time-resolved reflection of an ultra-high frequency pulse propagating along the microstrip line, occurring due to a time-modulated distributed impedance. Importantly, our experimental system can be extended to two dimensions, where new ideas[32] can be explored.

For a strong time-reflection at microwave frequencies, the change in the characteristic impedance due to the temporal event must be fast —within one to two cycles of the time-reflected waves. Consequently, we use high-speed photodiodes with switching times in the picosecond range to control the capacitive loading and achieve the desired bandwidth. The entire experimental setup is judiciously designed to maximize the available bandwidth in both states, such that we can study the propagation of very short pulses in the microstrip line. The electric length of the microstrip line is optimized to be as short as possible, so that the pulse always remains completely within the line during the temporal event. Such a unique experimental system allows us to explore the evolution of ultra-high frequency signals and observe time-reflections at 0.59 GHz created by an almost-instantaneous time-interface. Subsequently, we study the propagation of a hybrid two-peak asymmetric pulse and demonstrate the time-reversal nature of the time-reflected signal, along with its frequency translation arising from the conservation of momentum. Finally, we study the time-reflection of a chirped pulse with a phase structure, providing the first experimental evidence of the phase-conjugation nature of time-reflected electromagnetic waves.

Apart from the exciting fundamental aspects of this study, our prototype system has important practical value. It employs realistic microwave circuit designs with surface mount high-speed photodiodes, demonstrating the viable potential of ultra-fast time-modulated microstrip circuits for nascent real-world applications in novel microwave pre- and post-processing systems, AI-driven navigation, and satellite communication platforms, including recently demonstrated applications in pulse shaping[33].

Results

Principles of operation

In this work, a reconfigurable periodically-loaded microstrip with rapidly switchable effective characteristic impedance models an abrupt change in the effective permittivity of the medium. A time interface is generated while a microwave pulse propagates within the microstrip, and the corresponding time-reflected and time-refracted (transmitted) signals are measured at the input and output, respectively.

Fig. 1a illustrates a 3D concept of our reconfigurable distributed microwave transmission line (DMTL) used to experimentally demonstrate time-refraction and time-reflection of a microwave pulse. The DMTL is designed to be periodically loaded with two parallel shunt capacitors, C_a and C_b. The second capacitor (C_b) is connected in series to a switch controlled by a high-speed photodiode. Both capacitors are terminated with conductive vias to the ground. Upon excitation by light (green optical trigger pulse), the high-speed photodiodes switch from an isolating OFF-state to a conductive ON-state, connecting the additional shunt capacitor C_b to the circuit. This reconfiguration changes the effective impedance of the microstrip from State 1 to a lower impedance value in State 2, generating a time-boundary, thereby giving rise to time-reflection (red reflected pulse) and time-transmission (black transmitted pulse) of the input (yellow input pulse) wave traveling within the medium.

It is essential that the change in the wave impedance occurs within one to two cycles of the EM wave. Here, with the picosecond rise times of the high-speed photodiodes, the time interface is much faster than the inverse of the operating bandwidth of the microwave pulse, enabling a near-instantaneous time-boundary. This effect is analogous to the spatial reflection from an abrupt spatial boundary, and it facilitates a sizeable ultra-high frequency time-reflected pulse at 0.59 GHz. In addition to fast rise times, the use of photodiodes enables almost perfect synchronization of each switch periodically loading the microstrip, with element-to-element spacing much smaller than the guided wavelength of the microwave pulse for an effective continuous transmission line medium within our frequency band of interest. With the optical trigger of each photodiode switch provided by a single laser diode source triggered by a single electronic control, a truly homogeneous time-switched medium is generated.

In one spatial dimension, the refraction and reflection by a temporal boundary is equivalent to the refraction and reflection by a spatial boundary. However, despite the similarity, the outcome is fundamentally different. Namely, a spatial interface conserves energy per photon (hence the frequency of the reflected and refracted waves is the same as that of the incident wave) and the total photon flux is conserved, whereas for a temporal boundary energy is not conserved but causality plays a major role. These give rise to several properties that distinguish time-reflected waves from spatially-reflected waves[1,6]. The first is time-reversal: the temporal boundary leads to time-reversal (phase conjugation) of the reflected wave. Fig. 1a illustrates this effect with a two-peak asymmetric pulse generated by the time interface occurring homogeneously in the medium. Observing the input pulse (yellow trace), we see that the higher amplitude peak lags behind the lower one, as the input pulse travels towards the top right in the positive x-direction. Upon activation of the time-boundary, we observe a back-reflected pulse (red trace) with the order of the peaks reversed: the low-amplitude peak now lags behind the higher one, as the direction of propagation of the reflected pulse is now towards the negative x-direction. This effect is completely different with a spatial boundary; namely, for a wave bouncing off a spatial discontinuity (spatial wall), the leading edge reaching the wall is the first one to get reflected and to be detected at the far left side of the microstrip.

The second property has to do with position. Whereas the reflection of a wave from a spatial boundary occurs at the position of the boundary, the time-refection from a time-boundary occurs everywhere in the medium simultaneously. Namely, the entire pulse inside the one-dimensional strip gets time-reflected at the same time. This distributed reflection effectively reverses the pulse in time: its trailing edge becomes the leading edge, and the leading edge becomes the trailing one.

The third property distinguishing time-reflected waves from their spatial analog is their sizeable spectral translation due to spatial translational symmetry, since the wave momentum is conserved everywhere across the time interface. Following[31], we derive the frequency translation due to a scattering event at the time interface based on a distributed circuit model of a microwave transmission line. For details of this derivation, see the Supplementary Information, Note 1. The frequency of the input wave (ω_1) is transformed to that of the reflected and transmitted waves (ω_2) as,

$$\omega_2 = \sqrt{\frac{C_1}{C_2}}\omega_1 = \frac{Z_2}{Z_1}\omega_1 \quad (1)$$

https://doi.org/10.1038/s41467-024-51171-6

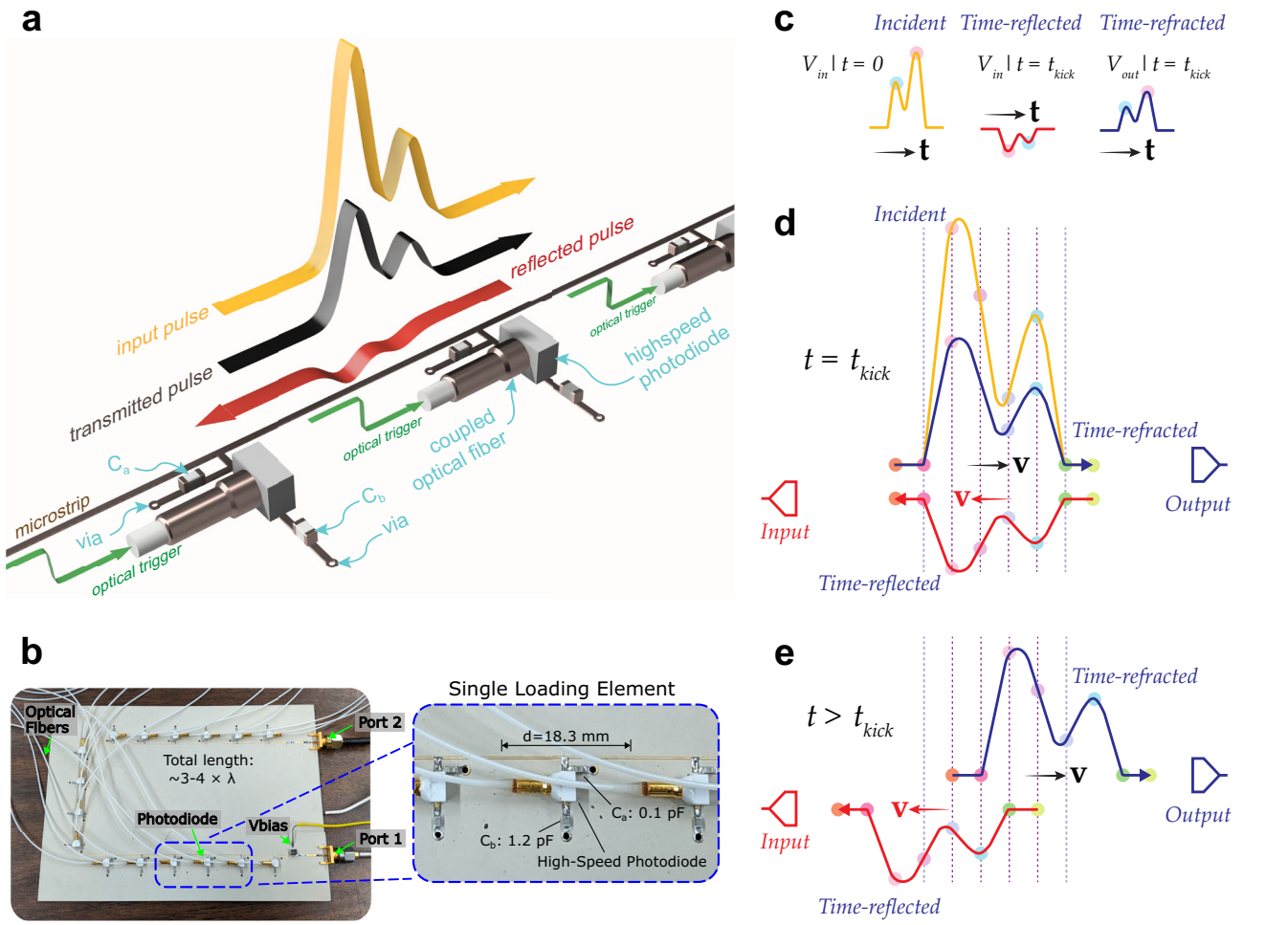

Fig. 1 | Impact of a time-boundary on a two-peak asymmetric pulse. **a** Conceptual 3D illustration. An input two-peak asymmetric pulse (yellow input pulse) with the smaller amplitude peak leading to the larger is propagating along a periodically-loaded microstrip transmission line. The effective impedance of the microstrip is modulated in time by high-speed photodiodes. The diodes are synchronized by simultaneous optical triggers (green optical trigger) delivered through the optical fibers from a single laser diode (not shown). Upon activation of the time interface, the input pulse is transformed into a time-refracted pulse (black time-refracted pulse) and a time-reflected pulse (red time-reflected pulse). The time-refracted pulse continues to travel in the same direction as the input, with the smaller amplitude peak still leading the larger, with reduced magnitude. The time-reflected pulse travels in the opposite direction: the larger amplitude peak now leads to the lower one, demonstrating the time-reversal property of time-crystals. **b** Photographs of the measured prototype and a single loading element with a surface mount high-speed photodiode. **c** The incident (yellow) pulse before, and the time-reflected (red) and time-transmitted (blue) pulses after the time-scattering event at $t = t_{\mathrm{kick}}$ demonstrating the time-reversal of the reflected pulse. **d** The incident, time-reflected, and time-refracted pulses exactly at the time-boundary event. The pulses are shown in the spatial domain, with the vertical dotted lines representing a spatial discretization and the colored circles representing fixed points in space along each signal. **e** The time-reflected (red) and time-refracted (blue) pulses propagating an equal distance from their original positions at the time-boundary event at $t > t_{\mathrm{kick}}$, while the incident pulse vanishes. The time-refracted signal inherits the order of peaks from incidence, so its lower peak enters the output port first. In contrast, the time-reflected signal enters the input port in reverse order (with its higher peak first).

where C_1, Z_1 and C_2, Z_2 are the loading capacitances and effective characteristic impedances of the DMTL in State 1 and State 2, respectively. This straightforward model immediately leads to the time-boundary reflection and transmission coefficients,

$$R = \frac{1}{2}\left(\frac{C_1}{C_2} - \sqrt{\frac{C_1}{C_2}}\right) = \frac{Z_2(Z_2 - Z_1)}{2Z_1^2} \tag{2}$$

$$T = \frac{1}{2}\left(\frac{C_1}{C_2} + \sqrt{\frac{C_1}{C_2}}\right) = \frac{Z_2(Z_2 + Z_1)}{2Z_1^2} \tag{3}$$

Fig. 1c provides a schematic illustration of the time-reversal phenomenon unique to time-boundary scattering of a two-peak asymmetric pulse. For simplicity, the example does not include the frequency translation effect. As shown in Fig. 1c, before triggering the time-boundary, the lower peak of the incident (yellow) pulse goes in front of the higher peak. Once the incident pulse is completely contained within the microstrip and the time-boundary is activated, the time-transmitted (blue) pulse appears, maintaining the same profile as the incident one but with a slight decrease in amplitude. Notably, the time-reflected (red) pulse becomes time-reversed compared to incidence—the higher peak will be measured before the lower one. The amplitude inversion of the time-reflected signal is due to the difference in the microstrip's impedance between the two states before and after the time-boundary, with a higher impedance in State 1 than State 2, leading to a negative time-reflection coefficient. Similar results were presented in ref. 31.

Fig. 1d, e depict a more detailed evolution of the time-reflection process. Panel d shows the incident, time-reflected, and time-refracted pulses strictly at the time-boundary event, to provide an intuitive understanding of this phenomenon. Precisely, when the time interface

is triggered, spatial boundaries appear locally at each discretized point of the incident signal simultaneously in time. The scattering event splits the incident signal into two: a time-reflected replica propagating from right to left (red velocity arrow) towards the input port and a time-refracted replica propagating left to right (blue velocity arrow) to enter the output port. Since effectively, at each point in space, the signal is nearly instantly transmitted and reflected by a spatial boundary, the tail end of the incident signal becomes the leading edge of the time-reflected signal, reversing the entire signal at each point in space at the exact same point in time.

Fig. 1e depicts the time-reflected and time-refracted signals after the time-boundary, which have now propagated an equal distance from their original positions after the time-boundary event. The colored circles in Fig. 1d, e represent fixed points in space along each signal, discretized accordingly to the vertical dashed lines. At $t = t_{kick}$, the circles are fully aligned, while at $t > t_{kick}$, they are equally offset to the left for the time-reflected pulse and to the right for the time-refracted pulse. The time-refracted (blue) pulse replicates the order of peaks of the original incident pulse, so the lower reflected peak enters the output port first, keeping the original first-in-first-out sequence of its colored markers. In contrast to the conventional reflection, the time-reflected (red) pulse enters the input port in reverse order (with its higher peak first or the first-in-last-out sequence of the markers).

These properties and theoretical derivations of the time-reflection and time-refraction off the time-boundary will now be studied in experiments in the following sections.

Design

The design of the time-reconfigurable periodically-loaded microstrip line follows standard design principles for reconfigurable DMTLs, with full details provided in Supplementary Information, Note 2. Here, only a brief description is presented. First, the microstrip parameters, element spacing, and capacitor loading values shown in Fig. 1a and described in the Principles of Operation section for State 1 ($C_1 = C_a$) and State 2 ($C_2 = C_a + C_b$) are determined to achieve the required effective impedance modulation from Z_1 to Z_2 for a measurable time reflection. In our study, the impedance is designed to modulate from $Z_1 = 60\,\Omega$ to $Z_2 = 40\,\Omega$ upon light activation of the photodiode switch. A total of 16 loading elements with a periodic spacing of $d = 18.3$ mm are chosen to accept the entire pulse within the microstrip during the time-boundary event, with the total microstrip length approximately three to four guided wavelengths long.

Next, to provide a modulation speed faster than the period of the signal to be scattered in order for a time-boundary to occur, the switchable capacitive loading shown in Fig. 1a and described in the Principles of Operation section is designed using a commercially available high-speed PIN photodiode. Compared to a 0.5 GHz pulse with a period on the order of 1 ns, the rise time of the photodiode is measured to be 311 ps, satisfying the modulation speed requirements of a time-boundary for this operating frequency range, and leading to a realizable prototype suitable for our time-boundary experiment. Further details of the switchable capacitive loading and high-speed photodiode design are provided in the Supplementary Information, Note 2. A picture of the fabricated and assembled prototype is shown in Fig. 1b.

Experimental validation

The fundamental effects of time-reflected waves described above, including time-reversal, phase conjugation, and spectral translation, are now demonstrated with time-boundary experiments using single, two-peak asymmetric, and chirped pulses. Specific details on the fabricated prototype, experimental setup, and the measured frequency response of the time-reconfigurable microstrip can be found in Supplementary Information, Notes 3 and 4, respectively.

The most critical aspect of this experiment is to synchronize the timing of the high-speed photodiode activation while the RF pulse is within the microstrip TL. To achieve this synchronicity, we use an Arbitrary Waveform Generator (AWG) with a sampling rate of 25 GSa/s to generate both the optical trigger and RF pulse. This coherence enables synchronization between the two signals, which can be tuned in 40 ps steps. Supplementary Fig. 5a in the Supplementary Information, Note 3, presents a block diagram of the procedure we use to generate the time reflection. First, we send a control signal from an AWG to a picosecond diode laser (Highland Technology T165-12) that generates an optical pulse with a carrier wavelength of 1550 nm and a picosecond rise time. The laser diode is coupled into an optical fiber and its optical pulse is then split evenly into 16 optical fiber channels, with each fiber controlling a high-speed photodiode periodically loading the microstrip. Assuming a stochastic uncertainty of the fiber length of ± 5 mm and a fixed refractive index of $n \approx 1.97$, gives a possible deviation within ±33 ps in synchronized timing across all switches, which is significantly shorter than the measured switching time (311 ps) and the carrier period of the microwave pulse (~2 ns). Hence, the optical pulses reach all 16 photodiodes at essentially the same time, generating a homogeneous and near-instantaneous change in the microstrip's effective impedance.

Along with the optical pulse, we send a microwave pulse into the microstrip from the same AWG. With a shorter path length and effective travel time to reach the microstrip, this probe pulse is carefully synchronized and slightly delayed from the optical control signal, such that the microwave pulse is entirely within the microstrip when the optical pulse reaches the photodiodes and activates the time-reflection. The microwave pulse interacts with a time-boundary, and we measure both the refracted (transmitted) and the reflected waves at both ends of the microstrip.

Time reflection of a single pulse

This section presents our simulated and measured results of both the time-reflected and time-refracted (transmitted) signals of a single Gaussian pulse with a full-width half-maximum (FWHM) bandwidth of 0.35 GHz scattered at a time interface.

Our system contains both spatial boundaries and a time-boundary. It is, therefore, essential to first explore the spatial boundaries, extract their features, and only then isolate the phenomena akin to the time-boundary, which is the purpose of this article. The results of the studies on the spatial boundaries and the extraction of the spatial and time-boundary coefficients are described in the Supplementary Information, Notes 5 and 6, respectively. With the spatial coefficients known, the time-boundary coefficients are extracted from the measured results and are now discussed. Figure 2a, b show the simulated and measured results of the time-reflected single Gaussian pulse referenced at the input voltage V_{in} and output voltage V_{out}, respectively. The time-boundary (TB1) is activated at $t = t_{kick}$ by modulating the characteristic impedance of the line from Z_1 to Z_2 when the pulse has fully entered but has yet to exit the microstrip trace. As mentioned previously, the total length of the microstrip line in State 1 is just long enough to contain the spatial spread of a single pulse, thus the pulse has traveled approximately halfway through the line before the time-boundary is activated.

Referring to Fig. 2a, we see the time-reflected pulse with negative amplitude due to the time interface event triggered at time $t_{kick} = 6.85$ ns. The time-boundary reflection and transmission coefficients, Γ_{TB1} and T_{TB1}, respectfully, are extracted using the method described in the Supplementary Information, Note 6, and are plotted along with the theoretical values in Table 1, showing good agreement. The theoretical coefficients are calculated using (2) and (3), with Z_1 and Z_2 equal to 60 and 40 Ω, respectively.

The slight discrepancy in the measured Γ_{TB1} is likely due to losses and dispersion in the measured prototype unaccounted for in the

https://doi.org/10.1038/s41467-024-51171-6

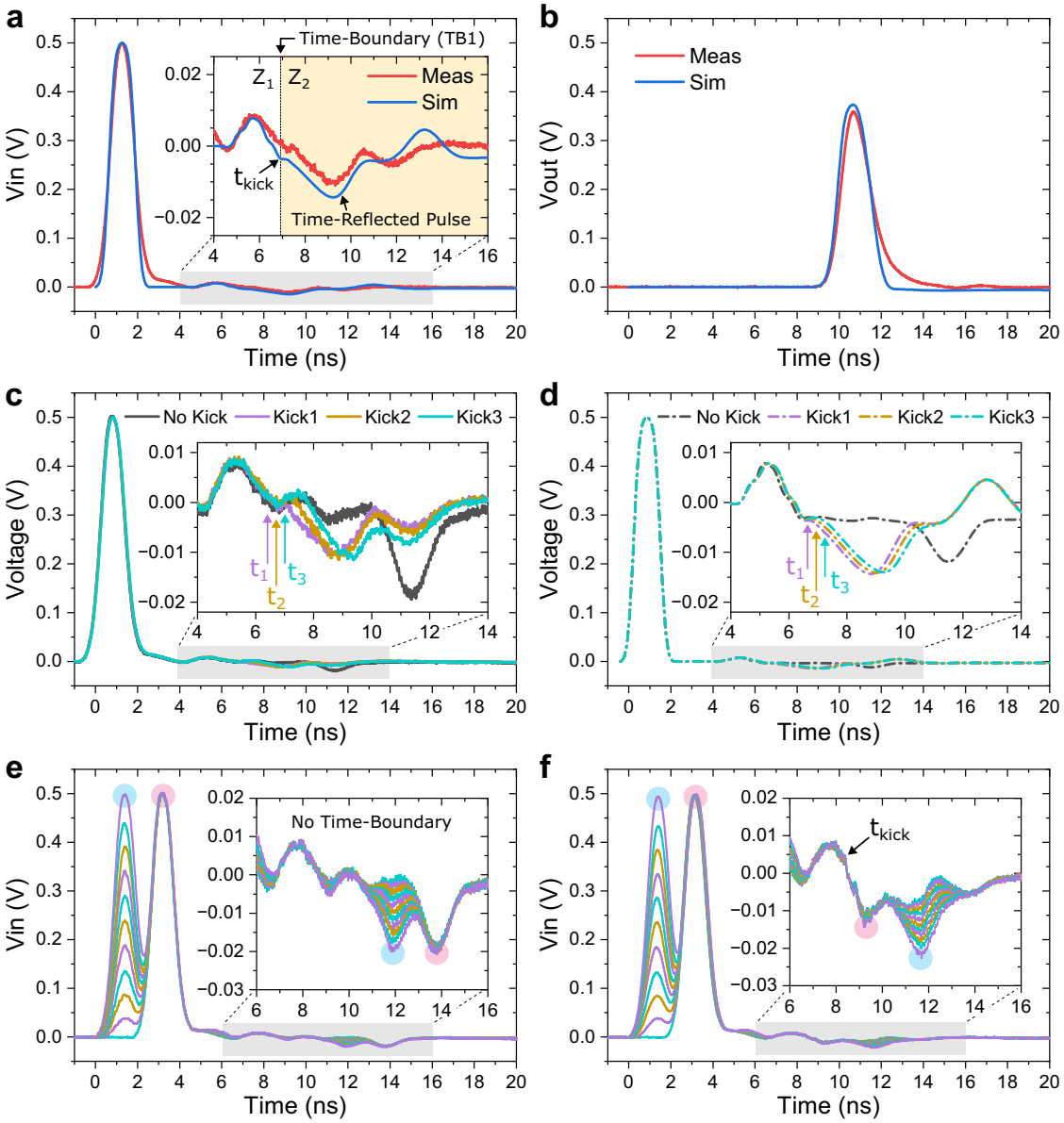

Fig. 2 | The measured and simulated response of the time-boundary experiments with a single Gaussian pulse (a–d), and the measured results of two sequential pulses fed into the microstrip line in which the amplitude of the first pulse is varied (e, f). a Response to a 0.35 GHz bandwidth Gaussian pulse referenced at the input V_{in} with a time-boundary generated by modulating the characteristic impedance of the line from Z_1 to Z_2 at time t_{kick} = 6.85 ns. **b** Output response referenced at V_{out}. **c** Measured response referenced at the input V_{in} while adjusting the triggering of the time interface with three different steps at t_1 = 6.47 ns, t_2 = 6.75 ns, and t_3 = 6.97 ns. **d** Simulated response corresponding well to measurement. **e** Demonstration of a spatial reflection without a time interface. **f** Demonstration of a time reflection with the time interface occurring at t_{kick} = 8.4 ns.

extraction process, as well as the finite switching speed of the photodiodes. While their switching speed was confirmed to be 311 ps (see Supplementary Information, Note 2), the period of a 350 MHz signal is ~2.9 ns. While the switching time is faster than the period of the wave traveling through the medium, a requirement for time-crystals[8], a faster switching time would lead to a more abrupt time interface and generate an increased reflection amplitude similar to an equivalent abrupt spatial interface, as explored in ref. 31.

To further demonstrate the pulse reflection and transmission is due to a time-boundary, Fig. 2c, d plot the measured and simulated response, respectively, of a single Gaussian pulse in which the triggering of the time-interface t_{kick} is varied. In Fig. 2c, we see that by delaying the triggering of the kick from t_1 to t_3, the time-reflected pulse is delayed accordingly. In Fig. 2d, we see a similar response in the simulated model, thus confirming this pulse is generated by the time-boundary event.

Table 1 | Time-boundary scattering coefficients

	Γ_{TB1}	T_{TB1}
Theory	−0.111	0.556
Simulation	−0.056	0.744
Measurement	−0.048	0.780

Time reflection of a two-peak asymmetric pulse

Figure 2e, f illustrate the experimental demonstration of the time-reversal property of reflected waves at a time-boundary discussed above. The figures show the measured input voltage versus time of a

https://doi.org/10.1038/s41467-024-51171-6

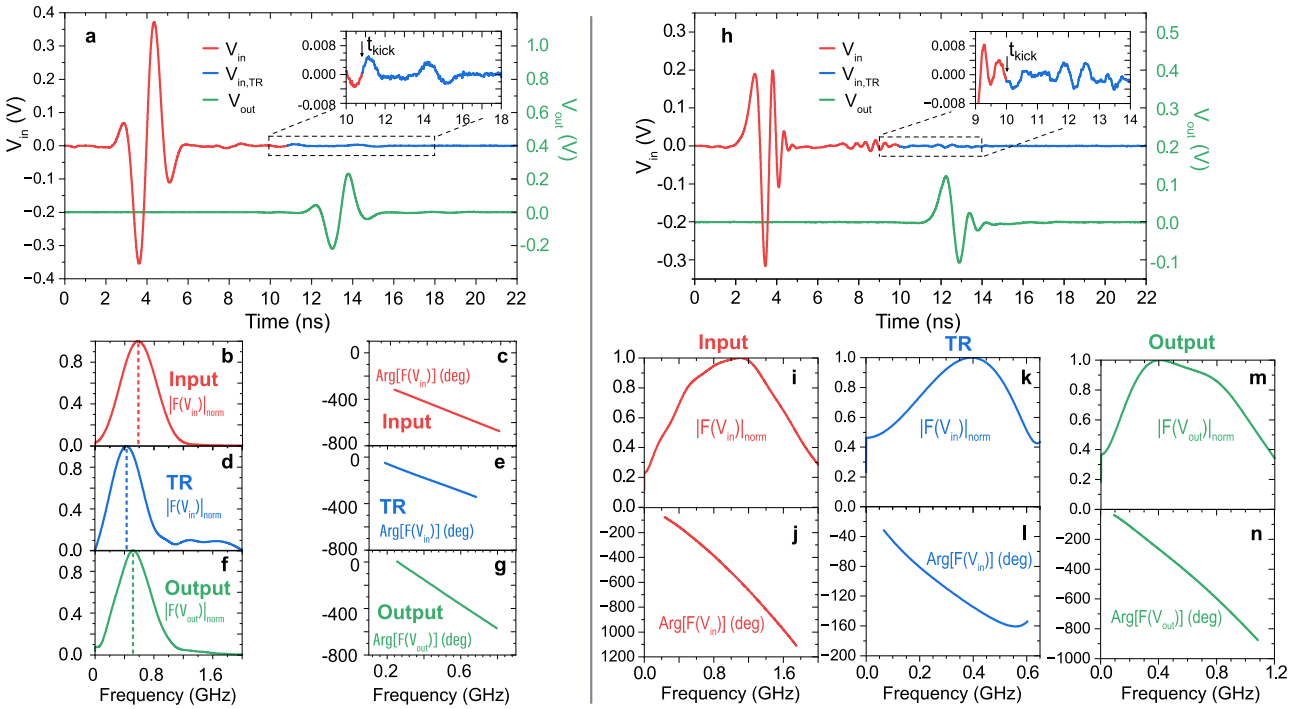

Fig. 3 | Measured results of EM pulses scattered at time interfaces with a single carrier Gaussian input pulse (a–g), and an input chirped pulse with a Gaussian envelope and nonlinear phase(h–n). a The results of a single carrier input pulse with linear phase (red trace) having a carrier frequency of 0.59 GHz incident at a time-boundary triggered at $t = t_{kick}$, with the corresponding time-reflected (blue trace) and transmitted (green trace) pulses to demonstrate frequency translation. **b**–**g** The corresponding results in the frequency domain. **h** The results of a chirped input pulse with nonlinear phase (red trace) scattered at a time-boundary triggered at $t = t_{kick}$, and the corresponding time-reflected (blue trace) and transmitted (green trace) pulses to demonstrate both frequency translation and phase-conjugation. **i**–**n** The corresponding results in the frequency domain.

two-peak asymmetric pulse fed into the microstrip and the corresponding reflection signals without (e) and with the time interface (f). By varying the amplitude of the first pulse, it is clear that (e) demonstrates a spatial reflection, i.e., the leading pulse is the first to reflect due to the impedance mismatch at the output and return to the input. In contrast, by applying a time-boundary at time $t_{kick} = 8.4$ ns, the time at which the pulse has fully entered the microstrip line but has yet to exit, (f) demonstrates a time reflection. Here, the leading input peak becomes the lagging peak due to the time reversal property of the time interface, a homogeneous and near-instantaneous change in the effective characteristic impedance of the microstrip. Likewise, after the time-boundary, the lagging input pulse becomes the leading peak of the reflected wave. The FWHM bandwidth of each peak is approximately 0.4 GHz.

Frequency translation resulting from a time-boundary

To demonstrate frequency translation at a time-boundary with our prototype, the time reflection and transmission of an input Gaussian pulse with a single carrier frequency was measured. Time-gated Fourier transforms are applied independently over the input (red trace), reflected (blue trace), and transmitted (green trace) to extract their spectral and phase content, with the results plotted in Fig. 3a–g. The spectral phases versus frequency are plotted across the FWHM of each pulse.

The input pulse in the frequency domain is centered at 0.59 GHz. The time-reflected pulse is centered at 0.43 GHz, and the transmitted pulse is centered at 0.51 GHz. This is conclusive evidence of frequency translation in our prototype, and also demonstrates the reflection of an EM pulse with the highest-to-date frequency from an optically-controlled ultra-fast time interface. The frequency translation corresponds to an ω_2/ω_1 ratio of 0.74 and 0.88 for the time-reflected and time-refracted waves, respectively, compared to the expected 0.67 from the theory presented above. This discrepancy is thought to be due to the finite length of the transmission line. Part of the pulse has begun to exit the microstrip line just before the photodiodes have completely turned on, triggering the time interface.

Regarding the spectral phase plots in Fig. 3c, e, g, the input pulse has a phase of −81.7 degrees at 0.59 GHz, the time-reflected pulse has a phase of −196.6 degrees at 0.43 GHz, and the transmitted pulse has a phase of −273.4 degrees at 0.51 GHz. Extrapolating the curves back to dc, the time-reflected signal exhibits a close to 180-degree shift compared to the input and time-refracted signals, corresponding to the theory prediction[31]. The slope of the time-reflected signal is also shallower than the input signal, indicating negative phase accumulation (counter-clockwise rotating phase vector) of the signal after the time-boundary. This interesting effect is explored in the next section.

Time reversal and phase conjugation demonstration

We now provide experimental evidence of the phase-conjugation nature of time-reflected waves[6–8,30]. From the voltage relationship (S18) derived in the Supplementary Information, Note 1, and considering the transmitted and reflected waves have the same angular frequency magnitude but are 180 degrees out of phase, i.e., $\omega_{2-T} = -\omega_{2-R}$ as per the treatment in ref. 1, the transmitted (time-refracted) and time-reflected waves can be split up accordingly:

$$V_{2-T} = V_{01} T e^{j(\omega_{2-T} t - kx)} = V_{01} T[\cos(\omega_{2-T} t - kx) + j \sin(\omega_{2-T} t - kx)] \quad (4)$$

$$V_{2-R} = V_{01} R e^{-j(\omega_{2-R} t + kx)} = V_{01} R[\cos(\omega_{2-R} t + kx) - j \sin(\omega_{2-R} t + kx)] \quad (5)$$

Here V_{2-T} and V_{2-R} represent the transmitted and time-reflected waves, respectively, while ω_{2-T} and ω_{2-R} represent the transmitted and reflected waves' angular frequency, respectively. These two waves have also been split into their quadrature components using the Euler identity ($e^{j\theta} = \cos(\theta) + j\sin(\theta)$) to highlight the difference in their phase rotation, i.e., the phase incurred by the waves as they travel forward in time, and their propagating direction in space.

Looking at the phase components, we see that the transmitted wave in (4) rotates counter-clockwise ($+j$), such that the wave incurs a positive phase as it propagates in the positive x direction ($\omega t - kx$). However, while the propagation direction of the time-reflected wave in (5) is in the negative x direction ($\omega t + kx$), similar to a spatially-reflected wave, the phase rotation for the time-reflected wave is clockwise ($-j$), such that the wave incurs a negative phase as it propagates. This is distinct from a spatially-reflected wave, such that the time-reflected wave is essentially a time-reversed wave, with phase conjugation in both space (kx) and time (ωt). This reversal of the phase in both space and time leads to the phase of the time-reflected wave reversing as the wave travels backward in space and forwards in time, and any phase incurred in the wave before the time-reflection is reversed in the time-reflected wave after the time-reflection. Further details on the comparison between spatially-reflected and time-reflected waves are provided in the Supplementary Information, Note 7.

To measure this time-reversal property, a chirped pulse with a Gaussian envelope and nonlinear phase is sent into our microstrip prototype and then time-reflected. The details of the input chirped pulse can be found in the Supplementary Information, Note 8. The experimental results are plotted in Fig. 3h–n. Again, frequency translation of the input pulse is observed, as expected, and the phase versus frequency of both the input and transmitted pulses have a negative slope. However, the phase of the time-reflected pulse has a positive slope, indicating phase-conjugation of the reflected wave.

Discussion

We experimentally demonstrate the time-reflection and time-refraction of electromagnetic waves from a broadband microwave pulse with the highest-to-date carrier frequency of 0.59 GHz due to an optically controlled ultra-fast time interface. The design and implementation of this time-boundary is enabled by a reconfigurable periodically-loaded microstrip transmission line capable of achieving near-instantaneous change in its effective impedance between two states using commercially available high-speed photodiodes with picosecond switching rates. The prototype is optimized to incorporate advanced yet realistic and accessible design solutions with practical advantages for real-world applications in future microwave systems. Good agreement between theory, simulation, and measurement is shown, validating the unique properties of time-reflected waves at microwave frequencies, including the time-reversal, frequency translation, and phase-conjugation nature of time-reflected waves. Last but not least, our system can be extended to two spatial dimensions, where it was predicted that a wave incident at a spatial interface between a dielectric medium and a medium undergoing an abrupt change in its refractive index will exhibit highly enhanced time-reflection and time-refraction[32]. These effects are strongly enhanced at the vicinity of the critical angle for total internal reflection.

Data availability

The data supporting the results of this work are available at the Purdue University Research Repository (PURR) and can be accessed at https://doi.org/10.4231/W2W3-8H49.

Code availability

The code supporting the results of this work is available at the Purdue University Research Repository (PURR) and can be accessed at https://doi.org/10.4231/W2W3-8H49.

References

1. Mendonça, J. T. & Shukla, P. K. Time refraction and time reflection: two basic concepts. *Phys. Scr.* **65**, 160–163 (2002).
2. Galiffi, E. et al. Photonics of time-varying media. *Adv. Photon.* **4**, 014002 (2022).
3. Zhou, Y. et al. Broadband frequency translation through time refraction in an epsilon-near-zero material. *Nat. Commun.* **11**, 1–7 (2020).
4. Shaltout, A. M., Kildishev, A. V. & Shalaev, V. M. Time-varying metasurfaces and Lorentz non-reciprocity. *Opt. Mater. Express* **5**, 2459–2467 (2015).
5. Morgenthaler, F. R. Velocity modulation of electromagnetic waves. *IRE Trans. Microwave Theory Tech* **6**, 167–172 (1958).
6. Biancalana, F., Amann, A., Uskov, A. V. & O'Reilly, E. P. Dynamics of light propagation in spatiotemporal dielectric structures. *Phys. Rev. E* **75**, 046607 (2007).
7. Lerosey, G. et al. Time reversal of electromagnetic waves. *Phys. Rev. Lett.* **92**, 193904 (2004).
8. Lustig, E., Sharabi, Y. & Segev, M. Topological aspects of photonic time crystals. *Optica* **5**, 1390–1395 (2018).
9. Zurita-Sánchez, J. R., Abundis-Patiño, J. H. & Halevi, P. Pulse propagation through a slab with time-periodic dielectric function ε(t). *Optics Express* **20**, 5586 (2012).
10. Shaltout, A. M., Fang, J., Kildishev, A. V. & Shalaev, V. M. Photonic time-crystals and momentum band-gaps. In *Conference on Lasers and Electro-Optics* (CLEO) (Optica, 2016).
11. Zurita-Sánchez, J. R., Halevi, P. & Cervantes-González, J. C. Reflection and transmission of a wave incident on a slab with a time-periodic dielectric function e(t). *Phys. Rev. A* **79**, 053821 (2009).
12. Reyes-Ayona, J. R. & Halevi, P. Observation of genuine wave vector (k or β) gap in a dynamic transmission line and temporal photonic crystals. *Appl. Phys. Lett.* **107**, 074101 (2015).
13. Holberg, D. E. & Kunz, K. S. Parametric properties of fields in a slab of time-varying permittivity. *IEEE Trans. Antennas Propag.* **14**, 183–194 (1966).
14. Lyubarov, M. et al. Amplified emission and lasing in photonic time crystals. *Science* **377**, 425–428 (2022).
15. Wang, X. et al. Metasurface-based realization of photonic time crystals. *Sci. Adv.* **9**, 1–8 (2023).
16. Dikopoltsev, A. et al. Light emission by free electrons in photonic time-crystals. *Proc. Natl. Acad. Sci. USA.* **19**, 1–7 (2022).
17. Shaltout, A. M., Kildishev, A. V. & Shalaev, V. M. Evolution of photonic metasurfaces: from static to dynamic. *J. Opt. Soc. Am. B* **33**, 501–510 (2016).
18. Shlivinski, A. & Hadad, Y. Beyond the Bode-Fano bound: wideband impedance matching for short pulses using temporal switching of transmission-line parameters. *Phys. Rev. Lett.* **121**, 204301 (2018).
19. Gaxiola-Luna, J. G. & Halevi, P. Temporal photonic (time) crystal with a square profile of both permittivity ε(t) and permeability μ(t). *Phys. Rev. B* **103**, 144306 (2021).
20. Sharabi, Y., Dikopoltsev, A., Lustig, E., Lumer, Y. & Segev, M. Spatiotemporal photonic crystals. *Optica* **9**, 585–592 (2022).
21. Apffel, B., Wildeman, S., Eddi, A. & Fort, E. Experimental implementation of wave propagation in disordered time-varying media. *Phys. Rev. Lett.* **128**, 094503 (2022).
22. Jaffray, W., Saha, S., Shalaev, V. M., Boltasseva, A. & Ferrera, M. Transparent conducting oxides: from all-dielectric plasmonics to a new paradigm in integrated photonics. *Adv. Opt. Photonics* **14**, 148–208 (2022).
23. Lustig, E. et al. Photonic time-crystals - fundamental concepts [Invited]. *Opt. Express* **31**, 9165–9170 (2023).
24. Liu, T., Ou, J.-Y., MacDonald, K. F. & Zheludev, N. I. Photonic metamaterial analogue of a continuous time crystal. *Nat. Phys.* **19**, 986–991 (2023).

25. Kinsey, N. et al. Epsilon-near-zero Al-doped ZnO for ultrafast switching at telecom wavelengths. *Optica* **2**, 616–622 (2015).
26. Caspani, L. et al. Enhanced nonlinear refractive index in ε-near-zero materials. *Phys. Rev. Lett.* **116**, 233901 (2016).
27. Lustig, E. et al. Towards photonic time-crystals: observation of a femtosecond time-boundary in the refractive index. In *Conference on Lasers and Electro-Optics (CLEO)* 1–2 (Optica, 2021).
28. Lustig, E. et al. Time-refraction optics with single cycle modulation. *Nanophotonics* **12**, 2221–2230 (2023).
29. Saha, S. et al. Photonic time crystals: a materials perspective [Invited]. *Opt. Express* **31**, 8267 (2023).
30. Bacot, V., Labousse, M., Eddi, A., Fink, M. & Fort, E. Time reversal and holography with spacetime transformations. *Nat. Phys.* **12**, 972–977 (2016).
31. Moussa, H. et al. Observation of temporal reflections and broadband frequency translations at photonic time-interfaces. *Nat. Phys.* **19**, 863–868 (2023).
32. Bar-Hillel, L. et al. Time-refraction and time-reflection above critical angle for total internal reflection. *Phys. Rev. Lett.* **132**, 263802 (2024).
33. Galiffi, E. et al. Broadband coherent wave control through photonic collisions at time interfaces. *Nat. Phys.* **19**, 1703–1708 (2023).

Acknowledgements

The work of T. R. Jones, A. V. Kildishev, and D. Peroulis is supported by the AFOSR under FY21-MURI award number FA9550-21-1-0299 (Dr. Arje Nachman, Program Manager). The work of M. Segev is also supported by the AFOSR under Grant No. FA8655-22-1-7256, also with Dr. Arje Nachman as the program manager.

Author contributions

T.R.J. did the design, fabrication, and all the experiments. All authors contributed to all other aspects of this work: conceptualization, data analysis, writing the manuscript, etc.

Competing interests

The authors declare no competing interests.

Additional information

Supplementary information The online version contains supplementary material available at https://doi.org/10.1038/s41467-024-51171-6.

Correspondence and requests for materials should be addressed to Dimitrios Peroulis.

Peer review information *Nature Communications* thanks Fabio Biancalana, Peter Halevi, and the other, anonymous, reviewer(s) for their contribution to the peer review of this work. A peer review file is available.